

High-speed odour sensing using miniaturised electronic nose

🔗 Nik Dennler,^{1,2,†} 🔗 Damien Drix,¹ 🔗 Tom P. A. Warner,^{3,4}
🔗 Shavika Rastogi,^{1,2} 🔗 Cecilia Della Casa,³ 🔗 Tobias Ackels,^{3,5}
🔗 Andreas T. Schaefer,^{3,4} 🔗 André van Schaik,² 🔗 Michael Schmuker,^{1,6,*}

¹Biocomputation Group, University of Hertfordshire, Hatfield AL10 9AB, United Kingdom

²International Centre for Neuromorphic Systems, Western Sydney University,
Kingswood 2747 NSW, Australia

³Sensory Circuits and Neurotechnology Laboratory, Francis Crick Institute,
London NW1 1AT, United Kingdom

⁴Department of Neuroscience, Physiology and Pharmacology, University College London,
London WC1E 6BT, United Kingdom

⁵Sensory Dynamics and Behaviour Lab, Institute of Experimental Epileptology and
Cognition Research (IEECR), University of Bonn Medical Center, 53127 Bonn, Germany

⁶BioML Research Services, Berlin, Germany

† E-mail: dennler@proton.me

* Corresponding author; E-mail: m.schmuker@biomachinelearning.net

Animals have evolved to rapidly detect and recognise brief and intermittent encounters with odour packages, exhibiting recognition capabilities within milliseconds. Artificial olfaction has faced challenges in achieving comparable results — existing solutions are either slow; or bulky, expensive, and power-intensive — limiting applicability in real-world scenarios for mobile robotics. Here we introduce a miniaturised high-speed electronic nose; characterised by high-bandwidth sensor readouts, tightly controlled sensing parameters and powerful algorithms. The system is evaluated on a high-fidelity odour delivery benchmark. We showcase successful classification of tens-of-millisecond odour pulses, and demonstrate temporal pattern encoding of stimuli switching with up to 60 Hz. Those timescales are unprecedented in miniaturised low-power settings, and demonstrably exceed the performance observed in mice. For the first time, it is possible to match the temporal resolution of animal olfaction in robotic systems. This will allow for addressing challenges in environmental and industrial monitoring, security, neuroscience, and beyond.

Introduction

The sense of olfaction is found all across the animal kingdom, and is crucial for survival and guiding behaviors such as navigation, food detection, predator avoidance, and mate selection [1, 2, 3, 4, 5, 6, 7]. Success in these tasks often hinges on the ability to swiftly and accurately detect and recognise scents [8, 9, 10, 11], particularly when dealing with odour plumes characterised by brief and intermittent encounters [12, 13] generated by turbulent dispersion processes [14, 15, 16]. Concentration fluctuations in odour plumes can exceed 100 Hz [17], while individual odour encounters can last single milliseconds or less [18] (see Fig. 1a). Many environmental cues are embedded in the fine structure of the odour plume [19, 20, 21], which

various organisms have evolved to use for their advantage. For instance, *Drosophila* olfactory receptor neurons can transduce odours in less than two milliseconds and resolve odour stimuli fluctuations at frequencies exceeding 100 Hz [22]. Similarly, honeybee projection neurons decode odour identity in tens of milliseconds after stimulus onset [23], while mosquitoes can identify CO₂ packets of just 30 ms [24]. A recent landmark study in mice has revealed their ability to discriminate rapid odour fluctuations, enabling them to distinguish temporally correlated from anti-correlated odours at up to 40 Hz, which facilitates source separation in complex environments [25].

Research on mobile olfactory robotics [26] has flourished over the last decade; driven by promising applications and solutions across various domains [27], and bootstrapping on the well established field of artificial olfaction[28]. The latter has demonstrated its effectiveness in domains where static and slow measurements are sufficient, such as the detection of hazardous gases or pollutants [29], spoilage alert systems [30], health monitoring [31], and food sciences [32]. However, many recent applications call for unmanned ground or aerial vehicles (UGV / UAV) to perform odour source localisation and navigation tasks [33, 34, 35, 27], which rely heavily on sensing the environment fast and efficiently, considering plume dynamics [36].

Typically, mobile olfactory robots incorporate electronic noses; devices that are characterised by arrays of multiple gas sensors and associated peripheral electronics [37]. They offer distinct advantages over conventional analytical methods such as Photoionization Detectors (PID) and mass spectrometers (MS), notably in terms of portability, power efficiency, cost-effectiveness, and sensitivity to a wide range of odours and volatile compounds. The most widely employed sensing components are Metal-oxide (MOx) gas sensors [38], which offer the significant advantage of a sensing layer that can be tuned through 1., modifications to its chemical structure, and 2., variations in operating temperature achieved by local heating, allowing for effectively detecting a diverse range of analyte classes. Their minimal requirements for

electronic peripheral components streamline sensor design, lower costs, and conserve valuable space. Further reductions in latency, form factor and power consumption were enabled through latest MEMS-based MOx sensors [39, 40], facilitating seamless integration into electronic circuits [41].

However, the relatively slow response and recovery times of MOx sensor electronic noses pose challenges for widespread adoption, and are prohibitive for many potential robotic applications [42]. For this reason, various studies have investigated sensor response times and tried to improve them. Recent advancements in both hardware [43, 44] and software [45, 46, 21, 47, 48, 49, 50, 51] have significantly reduced response and recovery times from the orders of hours or minutes [52] down to tens-of-seconds or seconds [49, 51]. Nevertheless, those timescales remain orders-of-magnitudes slower than what's observed for olfactory sensing in animals, potentially stalling progress on critical challenges in tracking of greenhouse gas emissions [53], ecological and environmental monitoring [54, 55], aerial-based wild fire detection [56] disaster management [57], and more.

In this work, we are pushing the limits of artificial olfaction with a high-speed, miniaturised electronic nose that can resolve odour pulses in the millisecond range. We propose an integrated e-nose design of MEMS-based MOx sensors and fast sampling periphery, as well as a set of powerful algorithms for control, sensing, and signal processing. We demonstrate the systems ability to operate at unprecedented temporal timescales when classifying short odour pulses, as well as when discriminating temporal characteristics of rapidly switching odour pairs. The challenge of deploying rapid and complex odour stimuli in a controlled and precise fashion [58] is overcome by using a high temporal-precision olfactometer setup, which most recently has been used for showcasing the temporal odour recognition capabilities in mice [25, 59].

We first elaborate on the proposed design of the electronic nose and the feedback control methods, with which we achieve thermal response times that allow for ultra-fast heater cycles

— orders-of-magnitudes faster than what is suggested in the literature. Later, we show that the electronic nose can successfully classify the odour of short pulses, with durations down to tens of milliseconds. This is achieved by rapidly switching the sensor heater temperature, then extracting phase-locked data features to train machine learning classifiers. Further, we demonstrate the system’s ability encode and infer temporal features in a task involving rapidly switching odour pairs, up to modulation frequencies of 60 Hz, which we show to match and even exceed the demonstrated capabilities of mice on equivalent tasks [25]. This is achieved by controlling the heater temperature to be constant, permitting for sensor response feature extraction from the frequency domain. Finally, we discuss our results and its implications, and identify some example use cases that may benefit highly from using fast sensing modalities.

Results

High-speed electronic nose and odour delivery system

We constructed a portable high-speed and high bandwidth electronic nose, which leverages the advantage of MEMS-based gas sensors and their rapid response times. We emphasised form factor and power consumption considerations that allow for sophisticated field measurements under space and power constraints, such as mobile robotic platforms[35]. Our design (Fig. 1c & Fig. S1a) consisted of the following elements: a microcontroller for data processing and storage, eight analogue metal-oxide MEMS gas sensors (Fig. 1d), associated analogue circuitry and data converters, and a combined pressure, humidity and temperature sensor.

Ideal MOx sensor operation requires the sensing site to be heated to several hundred degrees. The sensor response is highly dependent on the temperature and its variation over time. Previous studies have shown that a modulation of the sensor’s operating temperature often leads to better and faster gas discrimination performances [43], however the suggested sensor heater cycle durations were on the orders of seconds to minutes [43, 50, 60, 61, 62, 63]. Aiming to achieve

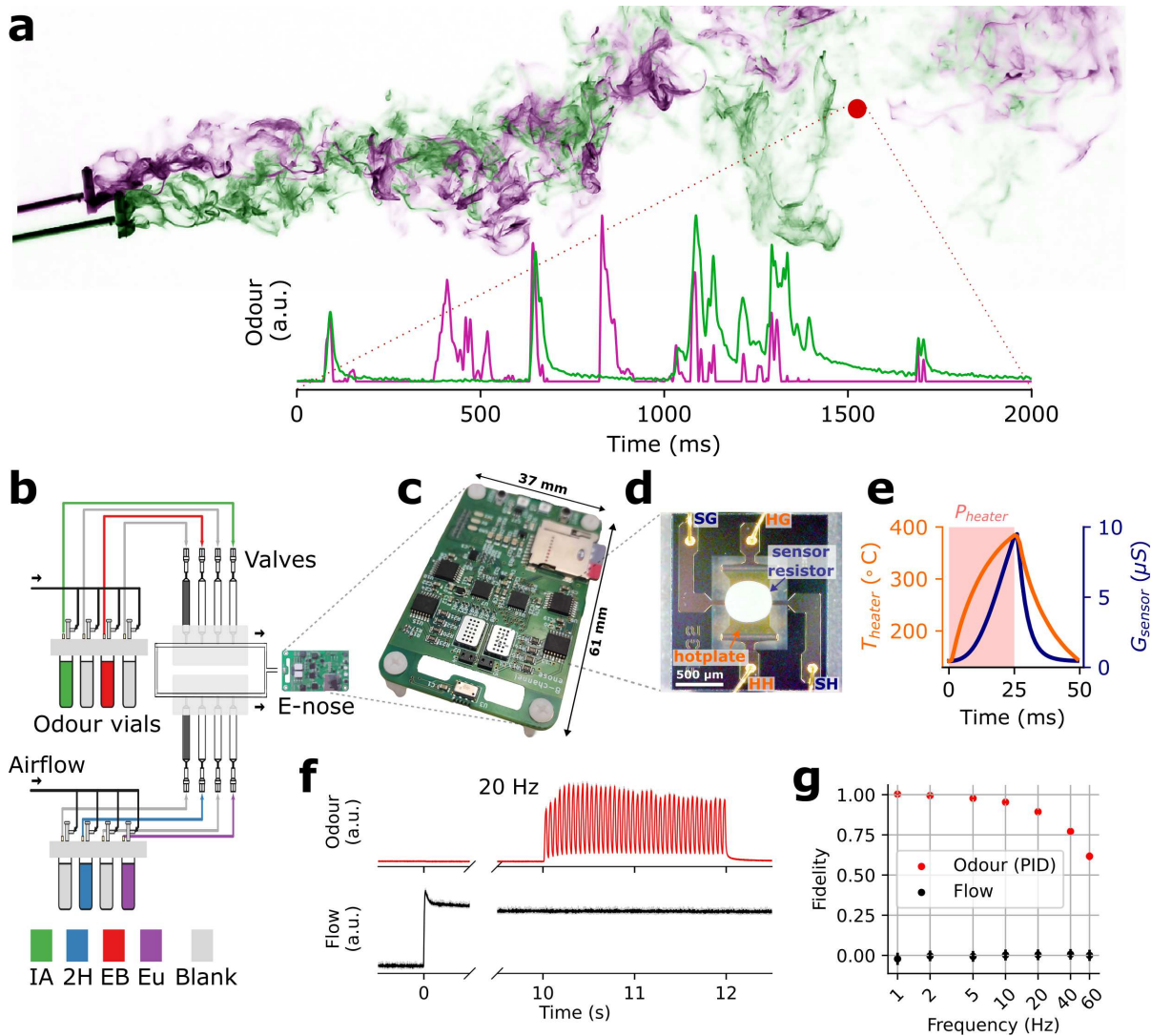


Figure 1: Electronic nose and odour delivery system. **a**, Decoding temporal information of odour plumes requires fast sensing. Top: Two sequential $TiCl_4$ smoke plume photographs, shifted and superimposed, kindly provided by Dr. Paul Szyszka. Bottom: Dual-PID recordings of source-separated odour plumes, from Ackels et al. [25]. Plume and sensor location (red) for illustrative purposes only. **b**, Experimental setup with odour delivery device and electronic nose. Adapted from Ackels et al. [25]. **c**, Electronic nose circuitry. **d**, Microscopy image of the MiCS-6814 NH_3 sensor with its housing removed. **e**, Heater modulation cycle in ambient air. **f**, PID and flow meter traces for a 20 Hz stimulus. Solid / faded (occluded) traces for mean / std. of five trials. **g**, Resulting olfactometer temporal fidelity, for various frequencies. Odourants abbreviations: IA: isoamyl acetate; EB: ethyl butyrate; Eu: cineol; 2H: 2-heptanone; blank: odourless control.

ultra-fast heater cycles,

our design couples each sensor with a separate temperature control loop, which samples the temperature and adjusts the hotplate current at high frequency. Fig. 1d shows a typical heater modulation cycle in ambient air, where the sensor resistance follows the hotplate temperature in a low-pass fashion. In our experiments, we used two different heater temperature control schemes: one that cycled between low and high temperature values (150 °C and 400 °C), and one at a constant high temperature (400 °C).

To provide odour stimuli to the e-nose, we used an odour delivery system that can reliably present gaseous odour samples with a bandwidth beyond 60 Hz, described earlier [25, 59] and depicted in Fig. 1b. The system was based on high-speed micro-valves and incorporated a flow compensation mechanism [25], ensuring exceptionally high temporal signal fidelity, and constant flow across the stimuli (Fig. 1f & Fig. 1g and Methods). As prototypical, simplistic high-frequency odour stimuli, we used square pulses of different duration and separation times. A set of odourants that resembles smells encountered in nature was considered: Ethyl butyrate (pineapple), isoamyl acetate (banana), cineol (eucalyptus) and 2-heptanone (cheese). The odourants were diluted in odourless mineral oil solvent. Additionally, we used two (identical) pure solvent samples as controls. The odours were presented as singular pulses with varying durations (10 ms - 1 s) and concentrations (20%-100%), and as correlated and anti-correlated odour pulse trains (1 s) at different modulation frequencies (2Hz - 60Hz).

Rapid heater modulation enables robust data features

While cycling the sensor heater temperature can yield better odour classification results, the cycle duration may be restricting the temporal bandwidth at which a stimulus can be resolved. In recent studies, we tested the effect of 150 ms duty cycles and found evidence for robust data features [64, 65]. In the current work, we leveraged our system's ability to rapidly modulate the

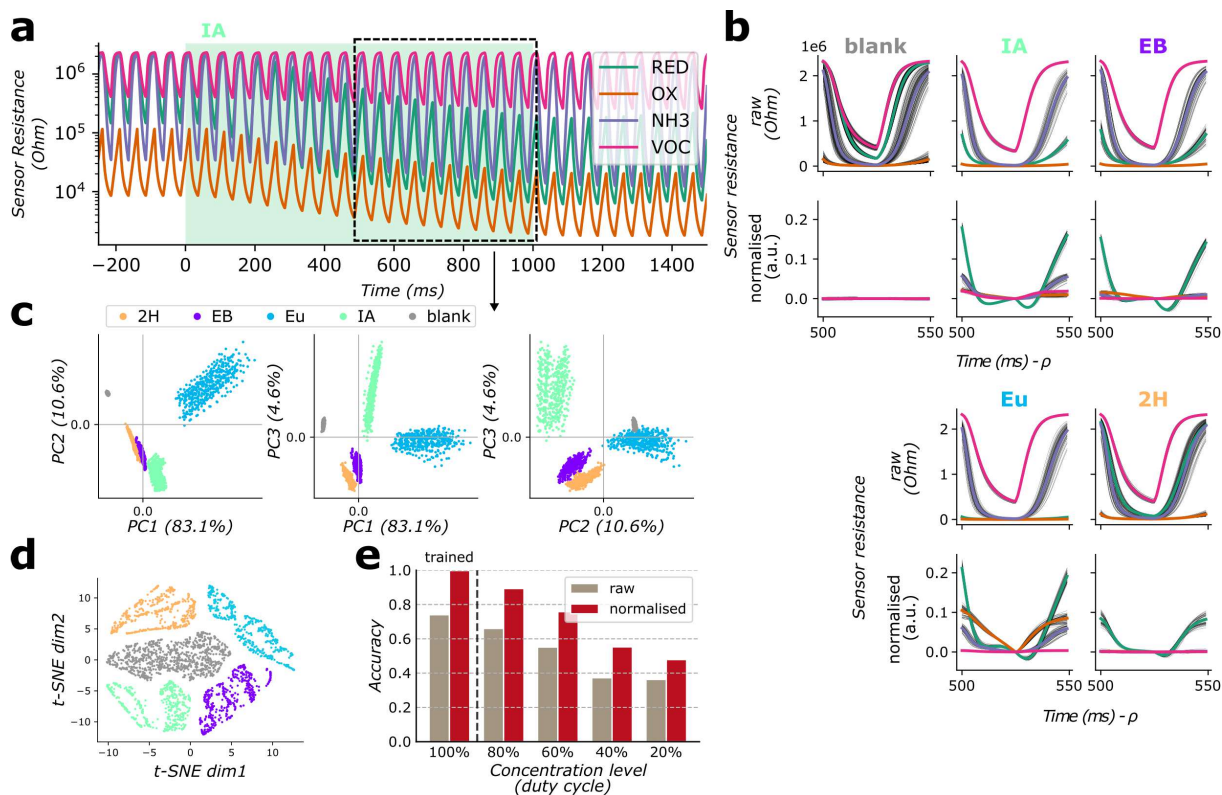


Figure 2: Rapid heater modulation enables robust data features. **a**, Sensor resistance of four MOx sensors with 20 Hz hotplate temperature modulation, responding to a 1 s odour pulse of isoamyl acetate (green background). **b**, 50 ms data feature for different gases, selected between 500 ms and 550 ms after odour pulse onset. Raw sensor response (upper) and normalised sensor response (lower, see Methods for normalisation procedure). Time shifted by cycle phase ρ w.r.t. odour onset, for visual guidance only. **c**, Principal component analysis (PCA), explained variance (most left) and projections, and **d**, t-distributed stochastic neighbour embedding (t-SNE) visualisation, for the set of normalised data features extracted between 500 ms and 1000 ms after odour onset. **e**, Accuracy scores for a k-nearest neighbours (k-NN) classifier trained on 50 ms data features from 1000 ms odour pulses at full concentration, and tested on 50 ms features from 1000 ms odour pulses at different concentration levels (tuned by adjusting the duty cycle of the micro-valves).

sensor temperature, and cycled the heater temperature between a low step at 150 °C and a high step at 400 °C with a period of 50 ms. Notably, this is orders-of-magnitudes shorter than what had been suggested in previous studies [63]. The resistance of the gas sensing elements closely tracks these changes in operating temperature (Fig. 1e & Fig. 2a), enabling us to extract gas

features that are phase-locked with the heater cycles for subsequent analysis and classification. For this purpose, we divided the continuous stream of gas sensor samples into 50 ms chunks aligned with the temperature cycles (Fig. 2b, upper row). The 50 ms data features further underwent pre-stimulus baseline normalisation and scaling (Fig. 2b, lower; from now on referred to as "normalised data feature"); for details see Methods).

For testing class discriminability and robustness to concentration fluctuations, data features were extracted by sampling four sensors between 500 ms and 1000 ms after the onset of a 1000 ms odour stimulus. Principal Component projections (Fig. 2c) and t-distributed stochastic neighbour embeddings (t-SNE) (and Fig. 2d) show distinct clustering that coincided with odour classes. Further, a k-nearest neighbours (k-NN) classifier was trained on data features of one second long odour pulses at full concentration (100%), and tested on features of one second long odour pulses at various concentrations (20% - 100%). The classification performance results are shown in Fig. 2e. Notably, for the normalised data feature, the model provided 100% classification accuracy at the trained concentration level, which remained at $(88.7 \pm 0.5)\%$ and $(81.2 \pm 0.6)\%$ when tested on 80% and 60% of the trained concentration level. Accuracy at lower concentration levels dropped significantly but remained well above chance. This is significantly better than what is achieved with the raw data feature (see Fig. 2e).

Time-resolved classification of millisecond odour pulses

In natural settings, odour bouts can be as brief as only milliseconds long. For an agent's successful interaction with the environment, this requires the ability to classify odours fast and robustly. We evaluated the ability of the electronic nose to classify odour pulses of various durations. A Support vector machine (SVM) with Gaussian radial basis function was trained on 50 ms data features, which were acquired from eight gas sensors throughout a 1000 ms odour stimulus at five concentration levels. Control trials ('blank') were included, obtained during a

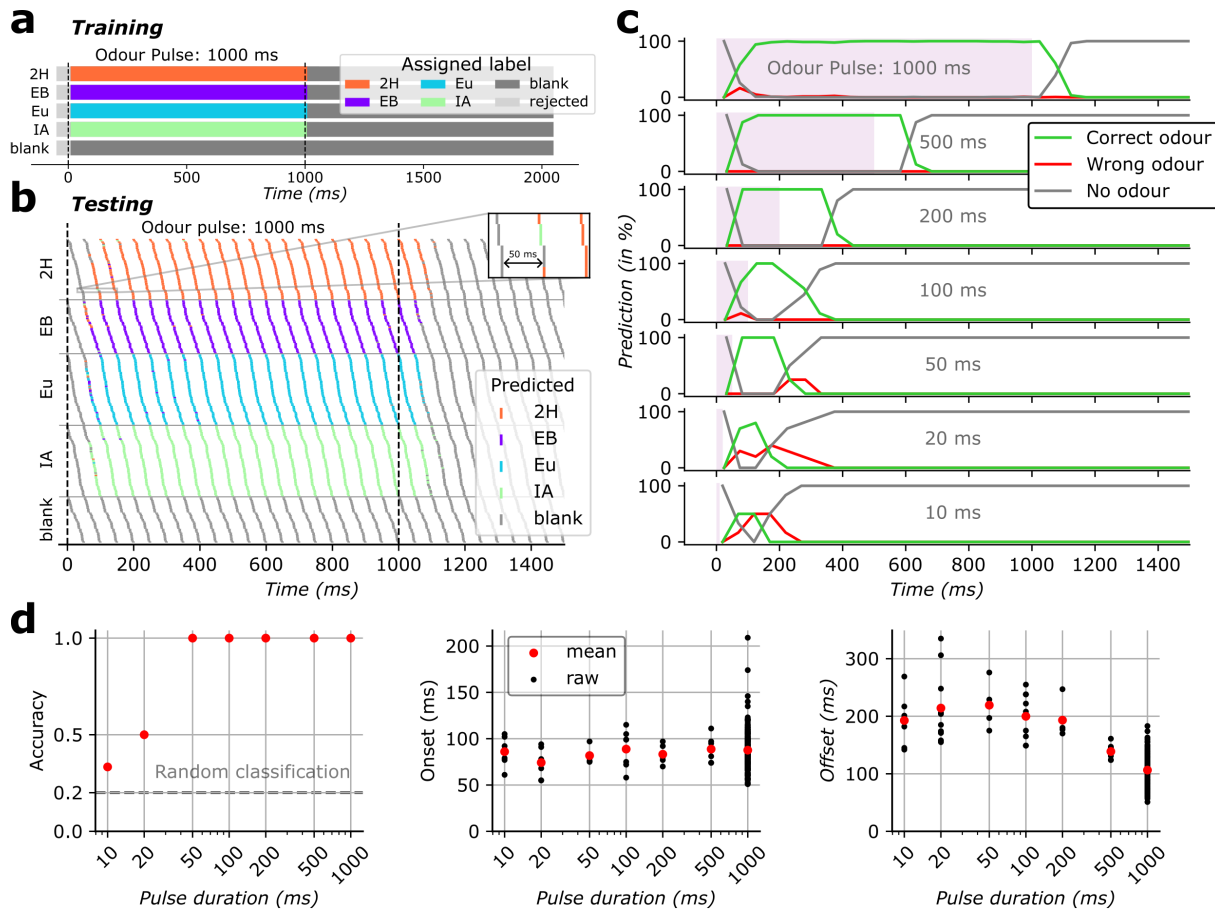


Figure 3: **Electronic nose can classify short odour pulses based on 50 ms data features.** **a**, Feature labels for the training set were phase aligned in relation to odour on- and offset. Features that overlapped with transition periods were not considered for training ("rejected", see Methods for parameters). **b**, Odour stimulus classification over time for odour pulses of various lengths (10 ms - 1000 ms, as predicted by a RBF-kernel SVM classifier trained on 50 ms features from 1000 ms second odour pulses. Shown here are 1000 ms pulses. For visual clarity only, the trials are sorted by odour, and within each odour are sorted by phase w.r.t. stimulus onset). **c**, Classification correctness over time (evaluated via the true odour presence), for different pulse durations. **d**, Test accuracy, onset time and offset time for the prediction over time described in **b & c**. Onset and offset were extracted using time-to-first non-'blank' and 'blank' prediction respectively, and shown here with respect to theoretical odour onset and offset.

1000 ms odourless mineral oil stimulation or immediately after odour pulses. See Fig. 3a for a depiction of the labelled features. The trained model was deployed to predict the odour presence over time during exposure to odour stimulations of various durations, ranging from 10 ms

to 1000 ms. Fig. 3b displays the predicted classes over time on the example of an 1000 ms odour pulse, where Fig. 3c summarises the predictions over time for all pulse durations.

From these predictions, the corresponding accuracy, onset times, and offset times were derived and shown in Fig. 3d. The classifier attained a 100% accuracy in predicting the correct class for odour pulse durations ranging from 1000 ms down to 50 ms, despite not having been trained on pulses shorter than 1000 ms. Accuracy dropped for 20 ms and 10 ms pulses but remained above chance level. Notably, the classifier accurately and rapidly predicted the recovery of the sensor site, indicating 'no odour' when no odour was present. The time required for the classifier to correctly identify the odour remained relatively consistent across odour pulse durations, with an average value of $(87 \text{ ms} \pm 20 \text{ ms})$. Following odour offset, the classifier robustly predicted 'no odour' within $(106 \text{ ms} \pm 24 \text{ ms})$ for 1000 ms odour pulses. For shorter durations, this time increased inversely proportional to the pulse duration, which can presumably be attributed to the sensor's integration time that may approach or exceed the duration of the short odour pulses.

Decoding temporal structure of rapidly switching odours

In the presence of multiple odours, detecting whether the odour encounters are correlated or not can help to infer whether they come from the same source or from separate locations [19]. Further, information about the encounter frequency can give rise to spatial source information [21]. It has been shown that mice can distinguish between correlated and anti-correlated odour pairs reliably up to correlation frequencies of 40 Hz [25]; a feat that has not yet been matched in robotic systems. Considering performance metrics based on similar tasks, here we explored the ability of the electronic nose to resolve temporal structure of odour stimuli. Rapidly alternating odour pairs were presented at frequencies between 2 Hz and 60 Hz for a duration of one second. We discriminated between two odour pulse trains being either in phase (correlated) or shifted

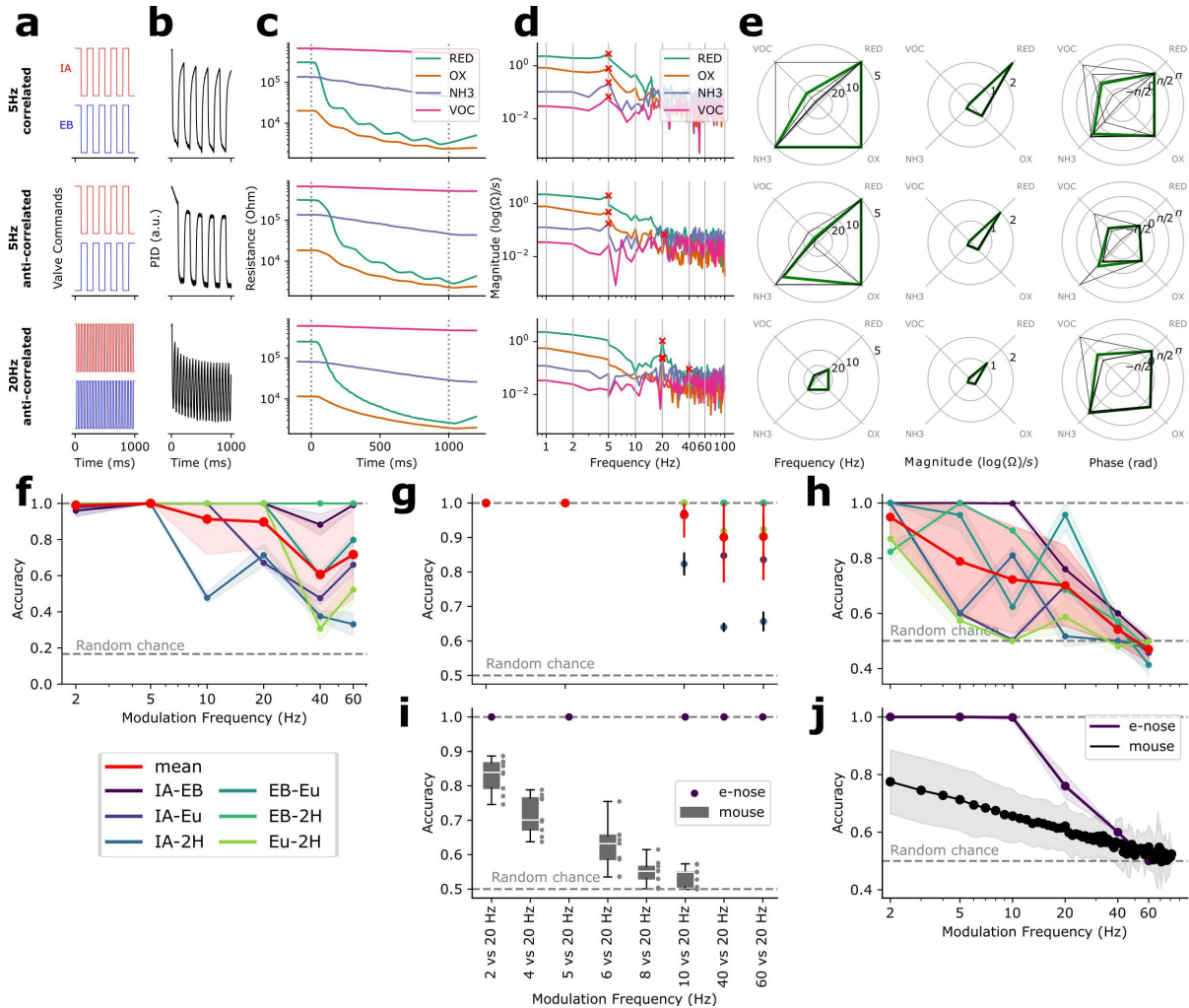


Figure 4: **Decoding temporal structure of rapidly switching odours.** **a**, Odour valve commands. **b**, PID response. **c**, Electronic nose response. **d**, Discrete Fourier Transformation (DFT) of first derivative of the sensor log-resistance. Crosses denote highest-magnitude peaks. DFT bin frequencies were rounded to nearest integers, for visual clarity only. **e**, Feature visualisation frequency, magnitude and phase of the dominant DFT peaks. Thick lines; means of corresponding trials, thinner lines; single trials. **f**, Class-balanced accuracies for modulation frequency classification. **g**, Accuracies for binary modulation frequency classification. **h**, Class-balanced accuracies for binary modulation mode classification (corr. vs. anti-corr.). **i**, Subset of *g* for IA-EB, for mouse performance comparison (described in detail in Ackels et al.[25]). **j**, Subset of *h* for IA-EB, for mouse performance comparison. Panels *a-e* show representative trials only. For *f-j*, electronic nose accuracy mean and SD (clipped at 1.0) arise from repeated training and testing with different random seeds.

by half a cycle (anti-correlated) (Fig. 4a). The resulting odour patterns follow the pulses rapidly (PID recordings in Fig. 4b).

While heater modulations lend themselves for extracting phase-locked data features and thus allowing for efficient odour classification, maintaining the sensor heater temperature constant instead allows for analysing the data in continuous time. Particularly when observing repeating patterns or complex temporal dynamics of a stimulus this may be advantageous, as the sensor response can be regarded in its frequency domain. Thus, for the following experiments, we operated four MOx sensors of the electronic nose under a constant hotplate temperature of 400 °C. The sensors responded to the stimuli by dropping their resistance at the pulse-train onset, with the stimulus modulation visually embedded in the response (Fig. 4c). We extracted data features by differentiating and logarithmically scaling the raw sensor response, followed by a discrete Fourier transform (DFT) (Fig. 4d). For each sensor, where the maximal magnitude is found, the frequency, the magnitude and the phase were extracted. This yielded a 12-dimensional data feature (Fig. 4e). A visual comparison of the features reveals distinct differences between correlated and anti-correlated pulse trains (top vs. middle), as well as between different frequencies (middle vs. bottom).

On those features, ensembles of Random Forest classifiers were trained for three tasks: 1. Decoding the modulation frequency of two odour pulse trains from a set of frequencies, 2. predicting the modulation frequency of two odour pulse trains from pairs of frequencies, and 3. decoding if two odours pulse trains are either correlated or anti-correlated. For the latter two tasks and a subset of the odours, a comparison with the mouse performance as detailed in Ackels et al. [25] is provided.

The test accuracies for the three tasks and all gas combinations are shown in Fig. 4f-h. For task 1, the data recorded with the electronic nose enables nearly perfect frequency classification (Fig. 4f) for modulation frequencies up to 5 Hz, then on average decreasing to (0.91 ± 0.20)

and (0.90 ± 0.15) for 10 Hz and 20 Hz respectively, and finally dropping to (0.61 ± 0.26) and (0.72 ± 0.25) for 40 Hz and 60 Hz respectively. For the pair-wise frequency classification (task 2, Fig. 4g), classification performance is perfect for modulation frequency pairs 2 Hz vs 20 Hz and 4 Hz vs 20 Hz, decreasing to accuracies of (0.97 ± 0.07) , (0.90 ± 0.13) and (0.90 ± 0.13) for the pairs 10 Hz vs 20 Hz, 40 Hz vs 20 Hz and 60 Hz vs 20 Hz, respectively. For discriminating correlated vs. anti-correlated pulse trains (task 3, Fig. 4h), it appears that the electronic nose, on average, enables high prediction scores of (0.95 ± 0.08) , (0.79 ± 0.20) , (0.72 ± 0.19) and (0.70 ± 0.14) for modulation frequencies of 2 Hz, 5 Hz, 10 Hz and 20 Hz, respectively. This drops to (0.54 ± 0.06) for 40 Hz and finally to (0.47 ± 0.05) for 60 Hz.

In Ackels et al. [25], the odour pair isoamyl acetate — ethyl butyrate (IA-EB) has been used to test the discrimination power of fast odour dynamics in mice. In the following, we consider the corresponding subset of the electronic nose recordings and compare them to the named study. For the pair-wise frequency classification (task 2, Fig. 4i), the electronic nose classification performance is perfect for all the tested modulation frequency pairs, from 2 Hz vs 20 Hz up to 60 Hz vs 20 Hz. Here, the mouse performed significantly worse — for the pair 2 Hz vs 20 Hz, the mouse accuracy score was (0.83 ± 0.05) and then progressively dropped down to (0.53 ± 0.03) for 10 Hz vs 20 Hz. Finally, considering the results from the phase prediction task (task 3, Fig. 4j), it appears that the electronic nose enables perfect prediction scores up to modulation frequencies of 10 Hz, which then steeply drops to an accuracy of (0.76 ± 0.05) for 20 Hz, (0.60 ± 0.00) for 40 Hz, and finally to chance level for 60 Hz. In comparison, the mouse scores (0.78 ± 0.11) at a modulation frequency of 2 Hz, linearly decaying in accuracy down to chance level at around 80 Hz.

In order to validate if the observed performance can be attributed to the odour signal, and not to potential artefacts caused by potential hotplate temperature variations (which may be caused by unnoticed flow fluctuations), we repeated the experiment using the hotplate temper-

ature signal (see Fig. S3i), as well as the PID responses (see Fig. S3m). In both cases, the analogous feature extraction and classification pipeline was performed, resulting in classification performances as displayed in Fig. S3j-l for the hotplate temperature, and Fig. S3n-p for the PID responses. The analysis confirmed that there was not enough information in the hotplate temperature response alone to classify the odourants with above chance performance. Further, using the PID response, which should be unaffected by potential flow fluctuations and is commonly used as a ground-truth measurement, nearly perfect accuracy scores were achieved for most gas combinations across the tested tasks.

Discussion

For many tasks and applications in robotics, natural and turbulent environments pose the challenge of highly dynamic and rapidly changing odour concentrations, which demands high temporal resolution odour sampling and processing. Intrigued by the exceptional speed at which animals process and respond to odours, we challenged the limits of artificial olfaction by introducing and evaluating a portable and low-power high-speed electronic nose. For this, we coupled an integrated design of MEMS-based MOx sensors and fast sampling periphery with a set of highly optimised algorithms for control, sensing, and signal processing. To assess its capabilities, the electronic nose was subjected to odour stimuli delivered through a high-bandwidth system. Odours were presented in the form of square pulses with varying durations and concentrations, or as pairs of pulse trains at varying frequencies and phase.

We demonstrated that the electronic nose can successfully infer the odour identity of single-odour pulses down to durations of 10 ms, albeit being trained on 1 s odour pulses only. This was achieved through modulating the sensor temperature with cycle periods of 50 ms, extracting and pre-processing the corresponding sensor response, then training and evaluating a classifier. Further, we demonstrate the electronic nose's ability to predict whether two-odour pulse trains

were correlated or anti-correlated up to switching frequencies of 40 Hz; matching or exceeding mice on the equivalent task. For tasks involving determining the odour switching frequency (multi-class and binary), we demonstrate a high performance up to 60 Hz, outperforming mice on equivalent tasks. For this, the sensor heaters were set to provide a constant temperature, which allowed an analysis of the data in the frequency domain.

Some valuable insights on task-specific sensing modes and sampling can be gained from those results. First, data windows that are phase-locked with ultra-short sensor temperature cycles appear to be a sensible choice when given the task of odour classification. The high sampling rate allows for a multi-dimensional data feature (here, 8 sensors times 50 samples per feature), which — together with the pre-stimulus normalisation procedure — successfully captures the odour-specific sensor response. In mammalian sensory neuroscience, the analogy would be the phase-coupling of spike-trains to the inhalation cycle, allowing the spike-timings to encode information about the odour identity, thus suggesting one "sniff" as the unit of olfactory processing [66]. Conversely, if the task is not classification but decoding temporal information about the odour stimuli, such as frequency or correlations, integrating the information across an artificial time window would limit the temporal resolution, hence recording continuously and without heat modulation might be the better choice. The ability of mammals to access temporal stimulus information at sub-sniff resolution has been demonstrated [25, 59], and shown to be relevant for behavioural tasks [25]. Those findings may suggest future experiments in which both modes are active simultaneously on separate sensor instances — continuously-sampled constant-temperature and time-integrated temperature-modulated — which could allow for extracting information about the temporal profile and the identity in parallel. Research on insect have suggested dual-pathway olfactory systems [67], which may facilitate the simultaneous extraction of odour identity and concentration information [68]. Such an approach might suggest elegant solutions to the olfactory cocktail party problem [69].

The proposed technology and its evaluation hold promise for tackling many real-world challenges that require rapid odour sensing. In particular, any instance of olfactory robotic solutions might currently be cut short in terms of performance; as for both UGVs and UAVs, the sensor response time dictates the maximum speed at which the agent can move while still obtaining spatially resolved measurements [54]. Thus, such applications may directly benefit from using the proposed sensor modalities, allowing for faster identification and localisation of odour sources. For instance, a recent work proposed swarms of nano quadcopters performing gas source localisation in indoor environments [70], and evaluated different search strategies. A decreased latency in detection and classification may not only assist in more efficient source localisation, but also in expanding the use case to multiple odours and more complex outdoor environments. Another recent study proposes odour sensing on drones for wildfire monitoring [56]. For detecting smoke; vision and gas sensors are fused, however the gas sensor update frequency is just 1 Hz. Given the intermittent and fine-structured nature of odour plumes, an improvement on sensing timescales could reduce false-negatives and aid in gaining critical time in localising the fire.

Beyond robotics, most applications in security still use static and relatively slow sensing platforms, for e.g. the odour-based detection of explosives [71] at airports. At checkpoints, fast and portable electronic noses could replace random spot checks with exhaustive controls, and thus minimise risk further. Further, recent investigations on mammalian olfactory-guided behaviour use head-mounted MOx sensors as control recordings [72]. Using a high-resolution data acquisition system — particularly one that matches the temporal capabilities of the subject — would allow for better data quality and hence could improve the resulting models.

In a related vein, neuromorphic information processing [73, 74] has seen much traction in recent years, where in particular the reduced latency, power consumption and data bandwidth have enabled highly optimised vision and auditory sensors [75, 76]. We suggest that the infor-

mation embedded in millisecond odour packets, together with the sparse and intermittent nature of odour plume encounters, makes the sense of olfaction an ideal candidate for neuromorphic sensing. We foresee that revealing the rapid nature of the sensors will further stimulate this field of research, motivating event-driven and asynchronous odour sampling [77], for MOx sensors [78, 79] and beyond [80, 81].

In conclusion, our study marks a groundbreaking advancement in electronic olfaction systems, demonstrating the ability to discern odours and decode odour patterns with unprecedented temporal precision in miniaturised low-power settings. Our findings unlock new possibilities for developing robotic systems capable of rapidly and precisely tracking odour plumes in compact and low-power environments, with the potential to transform electronic nose designs and their applications across various domains.

Data and code availability

The dataset and analysis code will be made publicly available upon publication, but can be provided earlier on request.

Methods

Electronic nose

Circuit board design

The electronic nose uses readily available components and is illustrated in Figure Fig. S1a. It features a *Raspberry Pi Pico* microcontroller and incorporates eight MEMS-fabricated MOx gas sensors of four different types, grouped into four packages.

The sensor packages comprise two *SGX Sensortech* MiCs-6814 sensors (sensors 1 and 5) and two *ScioSense* CCS801 sensors (sensors 2,3,4 and 6,7,8), capable of detecting a wide range of reducing and oxidising gases, including volatile odour compounds (VOCs), hydrocarbons,

carbon monoxide, hydrogen, nitrogen oxides, and ammonia. Figure Fig. 1c displays an optical microscopy image of the sensor structure. For sensing, the DC resistance across the sensing element is measured. The integrated micro-hotplates allow for operation at temperatures of up to 500 °C.

For controlling the micro-hotplates, eight operational amplifiers (2x *STMicroelectronics* TS924) are employed, and the sensor heater voltage is configured using two Digital-to-Analogue Converters (DACs), specifically the *Texas Instrument* DAC60004, which offer four channels each at 12 bits and 1 kHz. Additionally, two Analogue-to-Digital Converters (ADCs), the *Texas Instrument* ADS131M08, are used to read sensor and heater resistances. These are differential, simultaneous-sampling ADCs which read out the eight gas channels and the eight temperature channels in lockstep at 24 bits and 1 kHz (the two ADCs share the same clock). To monitor environmental conditions, a digital pressure-humidity-temperature sensor, the *TE Connectivity* MS8607, is included, which samples data at 24/16/24 bits and 50 Hz. Real-time data logging is facilitated through the inclusion of a microSD card. The device’s power needs, ranging from 1.2 W to 1.5 W, allow for multiple days of continuous operation on a pocket-sized battery pack, making it suitable for extended field recordings or robotic environments.

Sensor heater modulation

To implement controlled heater modulation, continuous measurement of the hotplate temperature and regulation of power delivered to the resistive heating element are essential. Each heater voltage V_{heat} was adjusted using a DAC and an associated amplifier, while the resulting current I_{heat} was monitored using an ADC in conjunction with a fixed-value sense resistor R_{sense} . From these two quantities one can compute the heater resistance $R_{\text{heat}} = V_{\text{heat}}/I_{\text{heat}}$ and dissipated power $P_{\text{heat}} = V_{\text{heat}}I_{\text{heat}}$. Because the device did not directly measure V_{heat} , the resistance calculated by substituting the known control and sense voltages $V_{\text{dac}} - V_{\text{sense}} \approx V_{\text{heat}}$ was subject to

errors, of which transient errors caused by lag and settling time in the DAC and amplifier were deemed the most significant. These affected the sample acquired immediately after a change in control voltage; therefore we used a Kalman filter [82] to estimate R_{heat} , setting the measurement uncertainty proportionally to the rate of change of the control voltage V_{dac} .

The kind of resistive heating element present in our design exhibits a quasi-linear relationship between hotplate resistance and temperature [83], so we used a linear model to map the heater resistance to a calculated hotplate temperature. The parameters of that linear model were set before recording the data by measuring the heater response to a series of power steps, and matching it with calibration data from the manufacturer’s datasheet, namely the nominal hotplate temperature delta above ambient air temperature at nominal heating power. This calibration procedure was repeated on an approximately weekly basis to account for the possible ageing of the sensors.

Achieving short temperature steps of a duration not much greater than the thermal time constant of the hotplate presented a number of challenges. Because the shortest steps consisted of only 25 samples (25 ms at 1 kHz), we employed a combination of open-loop and closed-loop control. In that scheme, we operated the heater at a constant voltage for the duration of each step. That voltage was selected based on a learned mapping between a desired temperature change, and the control voltage required to achieve it. We adjusted the mapping after every step to compensate for the effects of airflow and ambient temperature fluctuations, using a proportional controller with a relatively slow adaptation rate ($0.1 \text{ V } ^\circ\text{C}^{-1} \text{ s}^{-1}$). With this, fast and repeatable temperature modulation patterns can be obtained without introducing artefacts due to e.g. control loop oscillations.

For experiments with a constant heater temperature, achieving fast temperature changes was not an issue, but care was taken to avoid the artefacts caused by the DAC’s 12-bit quantisation of applied heater voltage. These quantisation steps of about 0.7 mV led to small but measurable

transients in the recorded sensor signal. Since these transients were in the same frequency band as the signals of interest, we decided to also keep the heater voltage constant during each stimulus. We adjusted it to eliminate the temperature error after each stimulus, which was sufficient since the thermal environment of the sensors changed only slowly.

Sensor responses to ambient air

The resistance of MOx sensors depends not only on the presence of gases, but also on the operating temperature. In heater cycle mode and odourless air (see Fig. 2b, left), the sensors exhibited nearly-exponential relationships between the recorded sensor resistances and the hot-plate temperatures in the range of 200 °C and 400 °C, with deviations at lower temperatures (see Fig. S1c). A small deviation can be observed between the trajectories corresponding to heating and cooling, however this may be attributed to uncertainties in estimating the temperature of the sensor, which is close to but not necessarily equal to that of the hotplate. The resistances returned to their initial values after a completed cycle, without significant hysteresis.

Odour delivery setup

Reagents

All odourants were obtained in their pure liquid form from Sigma-Aldrich, and contained in 15-ml glass vials (27160-U, Sigma-Aldrich). The odorants ethyl butyrate, isoamyl acetate and cineol were diluted 1:5 with mineral oil, while 2-heptanone was diluted 1:20 with mineral oil. 2-heptanone was diluted to a lower concentration as a 1:5 dilution saturated some of the gas sensors.

Olfactometer

Odours were presented using a custom made olfactometer capable of constructing temporally complex stimuli with temporal bandwidths of up to 500 Hz (Fig. 1d). This temporal olfactory

delivery device (TODD) has been outlined previously[25, 59]. The device consisted of 8 independent channels which contained either odour (diluted with mineral oil) or pure mineral oil. These 8 channels were grouped into two sets of 4. Each set of four consisted of an odour manifold, which contained odours or pure mineral oil in glass vials which were fed by a common air flow. Each channel in this odour manifold was fed into its own high speed valve on a separate valve manifold. Each high speed valve could be opened and closed at frequencies of up to 500 Hz. On each valve manifold, one of the channels containing pure mineral oil was set to remain open indefinitely, acting as a 'carrier' valve (grey valves in Fig. 1d). When a trial was triggered, this carrier valve flow was reduced in accordance with the amount of additional airflow generated by the other valves on the manifold, therefore maintaining a continuous rate of air flow through the system. In some cases, the carrier valve was not simply reduced, but was used to generate temporally complex airflow to compensate for the temporal patterns generated using the other valves in the system. Signals to the valves were convolved with a high frequency 500 Hz continuous signal, referred to as 'shattering'. This shattering was included as it has been previously found to improve the temporal fidelity of the resultant odour signal. The airflow to the TODD was maintained at a rate of 1 L/min using a custom closed loop-feedback flow controller.

Calibration

To ensure a continuous total airflow whilst maintaining a high signal fidelity, prior to the electronic nose recording session, the output of the olfactometer was measured with both a PID (200B miniPID, Aurora Scientific) and flowmeter (AWM5101VN, Honeywell). The PID was positioned a short distance away from the output of the olfactometer (> 2cm) and calibration trials were presented. These were selected in a way to making sure to cover all the different valve combinations of the experiment. The PID response to presented odours was measured

and the fidelity estimated. If the fidelity was found to be too low, the rate of flow into each channel was tuned to increase the fidelity. Next, the PID was replaced with the flowmeter, and the same selected calibration trials were presented. If the rate of flow varied during the trial presentation, the compensatory flow or carrier flow was modulated to return the net flow back to pre-trial levels. The flow through the odour valve was kept constant so as to not alter the odour signal fidelity. Airflow was modulated by altering the duty-cycle of the valve shattering. Once there was no visual change in the rate of flow between the trial and pre-trial levels the flowmeter was removed and the olfactometer was deemed to be calibrated.

Fidelity Calculations

For quantifying the olfactometers' temporal fidelity after calibration, we deployed single-odour pulse trains of different frequencies and obtained simultaneous PID and flow meter recordings. Here, the odourant Ethyl Butyrate was used, as its ionisation energy is well-suited for the used PID. In particular, at $t = 0$ s the carrier flow valves opened while odour valves remained closed, for a duration of 10 s. At $t = 10$ s the odour valve and odourless compensation valve deployed anti-correlated pulse trains of various frequencies, for 2 s (see Fig. S1a (left) for the 10 Hz example). The fidelity for each square pulse was calculated as the value of peak to trough, normalised to the peak to the baseline value. The fidelities shown in Fig. S1a (right) were computed as the mean and standard-deviation across all square pulses fidelities of a particular modulation frequency.

Experimental protocol

Electronic nose placement

The electronic nose was attached to a movable arm and fixed in place downstream of the olfactometer outlet, with a distance of approximately 3 cm from outlet nozzle to the gas sensors. To ensure that the gas flow reached all the sensors on the board, we fine-tuned the alignment of the

electronic nose with respect to the nozzle by trial-and-error until a strong response was obtained on all channels.

Heater modulation and odour delivery protocol

Three experiments with different sensor heater conditions were performed (see Fig. S1d for the conditions over time):

1. Sensor 1-8: 50 ms cycles between 150 °C and 400 °C.
2. Sensor 1-4: constant temperature of 400 °C, Sensor 5-8: 50 ms cycles between 150 °C and 400 °C.
3. Sensor 1-4: constant temperature of 400 °C, Sensor 5-8: 200 ms cycles between 150 °C and 400 °C (not used).

For each heater condition, odour stimuli of different pulse widths and concentrations (controlled by adjusting the shattering duty cycle of odour and mineral oil valves) were presented. After each odour stimulus, there was a 30 s recovery phase before the next stimulus onset. The set of different stimuli included:

- 4 odours + two control ('blank') vials, 50 repetitions 1 s odour pulses, at 100% concentration.
- 4 odours, 20 x 1 s odour pulses, at concentrations of 20%, 40%, 60%, and 80%.
- 4 odours, 5 repetitions of shorter odour pulses in the range [10, 20, 50, 100, 200, 500] ms, at 100% concentration.
- 2x6 odour pairs, 5 repetitions of 1 s anti-correlated pulse trains, at frequencies in the range [1, 2, 5, 10, 20, 40, 60] Hz, at 100% concentration.

- 6 odour pairs, 5 repetitions of 1 s correlated pulse trains, at frequencies in the range [1, 2, 5, 10, 20, 40, 60] Hz, at 100% concentration.

Within each experimental run, all the stimuli were presented in a fully randomised order. Fig. S1e shows the distribution of odours over time, binned in 1 h time intervals. A statistical χ^2 test was performed, confirming that the null hypothesis can't be rejected ($p = 0.364$), i.e. that the trials are in fact randomised. Importantly, the odour delivery protocol has not been synchronised with the sensor heater modulation phase.

PID recordings and odour onset/offset determination

A shortened version of the odour delivery protocol was deployed and recorded with the PID. Fig. S1f displays a PID response to a 1 s isoamyl acetate pulse. For all the odours, the mean and standard deviation of the pre-stimulus baseline were computed, and a threshold of 4 times the standard deviation (4σ) defined. This was used to estimate an upper bound for the time from theoretical stimulus onset to odour exposure at the sensing site, and a lower bound from theoretical stimulus offset to the purging of the sensor site. Fig. S1g displays all the extracted onset and offset values, indicating that the odour may reach the sensor as rapidly as in 10 ms, while the purging may take several hundreds of milliseconds. While PIDs are extremely fast, they too have a finite and odour dependent response time, thus the actual times may be shorter than this.

Pulse classification analysis

Feature extraction and validation

For evaluating what data features may be most suitable for the rapid classification of short odour pulses, we used experiment B, where sensor 1-4 were operated at a constant temperature of 400 °C, and sensor 5-8 employed heater cycles of 50 ms in the range of 150 °C and 400 °C.

Different sensor data features were used and evaluated: Data windows of 50 ms starting at a given time t relative to the stimulus onset at $t_{onset} = 0$ s were used to extract 1. raw data from constant heater sensors, 2. pre-stimulus ($t_{pre} = -5$ s) baseline subtracted data from constant heater sensors, 3. raw data from cycled heater sensors, and 4. pre-stimulus ($t_{pre} = -5$ s) baseline normalised data from cycled heater sensors. For the normalisation in the latter, the procedure is illustrated in Fig. S2c and described in the following. The extraction of the feature $G(\mathcal{D}_s, t)$ can be summarised as applying a chain of a sensor-wise logarithmic transformation and a maximum scaling, to both a 50 ms baseline data snippet before stimulus onset (here, $t_{pre} = -5$ s) and to a snippet at time t , and then computing their vector difference:

$$G(\mathcal{D}_s, t) = \frac{\log(H(\mathcal{D}_s, t))}{\max(\log(H(\mathcal{D}_s, t)))} - \frac{\log(H(\mathcal{D}_s, t_{pre}))}{\max(\log(H(\mathcal{D}_s, t_{pre})))} \quad (1)$$

Here, $H(\mathcal{D}_s, t)$ describes a kernel extracting data from the sensor recordings \mathcal{D}_s , starting at time t and stopping after one full heater cycle (e.g. 50 measurements). The sensor index is denoted as s .

The data was split into one set for training & validation, and one set for testing — with a ratio of 60% to 40% (see Fig. S2a). The former was used to train and validate a k-NN classifier using different features via cross-validation. The latter was used to evaluate the performance with the different features used.

Classifier training was performed on data features from sensor responses between 500 ms and 1000 ms after stimulus onset, where the stimuli were 1000 ms odour pulses of the gases 2H, EB, IA, Eu and blank, at 100% concentration. Testing was performed on equivalent data features, however now the stimuli concentration was sampled in the range [20, 40, 60, 80, 100]%, and the blank class was omitted. Fig. S2d displays the achieved performance using the different data features. The normalised cycled-heater data feature $G(\mathcal{D}_s, t)$ outperforms the other tested features, both in accuracy at 100% concentration, as well as for the reduced

concentrations. For clarity, Fig. 2e shows a subset of Fig. S2d.

Dynamic pulse classification

For the dynamic classification of short odour pulses, experiment A was used with all 8 sensors modulated on a 50 ms period between 150 °C and 400 °C. Again, a 60% vs. 40% split for training & validation vs. testing was performed, where the former was used to determine a suitable classifier and its hyper-parameters via cross-validation, while the latter served to evaluate the performance of the classifier (see Fig. S2b). Data features were extracted as described in Eq. (1). For training, the underlying data for the features are the sensor responses for the subsequent 2000 ms after the onset of 1000 ms odour stimuli, for concentrations in the range [20, 40, 60, 80, 100]%. The data features were labelled according to their time t as follows:

Algorithm 1 Training data labelling procedure

```

if  $t_{onset} \leq t < t_{offset} - \tau + d$  then
  Feature is fully within measurable odour pulse.
  if  $\mathcal{O}_{stimulus}$  is not 'blank' then
     $y = \mathcal{O}_{stimulus}$ 
  else
     $y = \text{'blank'}$ 
  end if
else if  $t_{offset} + d \leq t$  then
  Feature is fully after measurable odour pulse.
   $y = \text{'blank'}$ 
else
  Feature timing is ambiguous; exclude data feature from training set.
   $y = \text{'rejected'}$ 
end if

```

Here, $t_{onset} = 0$ ms and $t_{offset} = 1000$ ms are the stimulus onset and offset respectively, $\tau = 50$ ms is the feature duration, $d = 10$ ms is the upper bound stimulus delay as computed earlier, $\mathcal{O}_{stimulus}$ is the stimulus odour of the corresponding trial, and y is the prescribed label of the data feature in question. This procedure is illustrated in Fig. 3a.

For the normalised data features, several classification algorithms were trained and validated via five-fold stratified cross-validation. The best performing algorithm with corresponding hyper-parameters was selected, which here was a Support Vector Machine (SVM) classifier with radial basis function kernel [84] ($C = 1e3, \gamma = 1e-4$, balanced class weight). Ultimately, an ensemble classifier was composed from the five SVMs trained on each split.

For testing how well the trained classifier performs on shorter odour pulses, the features were extracted from sensor response data for the subsequent 2000 ms after the onset of odour stimuli of different durations, at 100% concentration. The stimulus durations fall within the set {10, 20, 50, 100, 200, 500, 1000}ms. For each data feature, the classifier predicted the odour, which is illustrated as a raster plot in Fig. 3b. The predicted odours y were compared against the actual stimulus odour $\mathcal{O}_{stimulus}$ and divided in predicting 'correct odour', 'wrong odour' and 'no odour', resulting in Fig. 3c. To extract the accuracy for each pulse duration, a confusion matrix was composed by — for each trial — comparing the most predicted non-blank class against $\mathcal{O}_{stimulus}$, across multiple trials. The on- and offset times correspond to the elapsed time from odour onset to first non-blank prediction, and from odour offset to first 'blank' prediction, respectively.

An analogous procedure was followed for testing the trained classifier on anti-correlated patterns of odour pairs, resulting in predictions over time, as shown in Fig. S2e & Fig. S2f.

Temporal structure analysis

For the temporal structure analysis, i.e. the determination of the frequency and the phase-shift of the two-odour pulse trains, the constant heater sensor data (i.e. sensors 1-4) of experiment B and C were used. In particular, experiment B was used for training and validation (i.e. finding and evaluating a suitable data feature and classification algorithm), where experiment C was used for testing, see Fig. S3a for an illustration.

Feature extraction

For each data trial, we extracted sensor data \mathcal{D}_s from $t = t_{onset}$ to $t = t_{offset} + b$, where $b = 100$ ms to account for the stimulus delay and potential sensor lag. The data was then log-transformed and differentiated before applying a discrete Fourier transformation $\mathcal{F}(\cdot)$, using the fast Fourier Transformation algorithm [85]:

$$L(\mathcal{D}_s) = \mathcal{F} \left(\frac{d}{dt} \log(\mathcal{D}_s) \right) \quad (2)$$

All triplets [frequency, magnitude, phase] were extracted, and sorted according to the magnitude. For each of the four sensors, the triplet with the highest magnitude was selected, collectively composing a 12-dimensional data feature.

Temporal structure classification

The data features and potential classifiers were evaluated on a 10-fold cross-validation using the training & validation data (i.e. experiment B) and the three different tasks described earlier. We decided on utilising a Random Decision Forest (RDF) classifier [86] (balanced class weight, $N_{tree} = 100$), and on using the same 12-dimensional data feature for all tasks. See Fig. S3b-d for an evaluation of the data features. For each cross-validation training split we trained a RDF classifier, then combined them to form an ensemble classifier for each task, which was finally evaluated on the testing data (i.e. experiment C). For the validation using hotplate temperature and PID data, the analogous pipeline was used, except that we omitted the log-transformation.

Comparing electronic nose performance with mouse performance

Performance analysis of the electronic nose to discriminate odour correlation structure was carried out in the style of a previously published experimental dataset (See Ackels et al. 2021 [25]). This allowed for a direct comparison of the electronic nose performance with that of mice during

an operant conditioning task. A complete description of the experimental conditions and data analysis can be found in the original paper. In brief, two cohorts of up to 25 mice were housed in a common home cage system [87] that is used as an automated operant conditioning setup. Mice were trained to discriminate perfectly correlated from perfectly anti-correlated odour stimuli switching at frequencies ranging from 2 Hz to 81 Hz. Task frequency was randomized from trial to trial. Odours were presented with a multi-channel high-speed odour delivery device similar to the one used in this manuscript. During a go/no-go task animal performance was rated based on their lick responses to $S+$ (rewarded) and $S-$ (unrewarded) stimuli. For roughly half of all mice, the correlated pattern was $S+$ and the anti-correlated pattern was $S-$. In the other half of the group this reward valence was reversed. All stimuli were 2 s long. A water reward could be gained by licking so that licking was detected for at least 10% of the stimulus time during an $S+$ presentation (a ‘Hit’). Licking for the same amount of time during $S-$ presentation resulted in a timeout interval of 7 s. In all other response cases, the inter-trial interval was 3 s and no water reward was delivered. All behavioural performance within a specified trial bin was calculated as a weighted average of $S+$ versus $S-$ performance:

$$\text{Performance} = \frac{(\text{Hit}/S+) + (\text{CR}/S-)}{2} \quad (3)$$

in which $S+$ is the total number of rewarded trials, $S-$ is the total number of unrewarded trials, Hit is the total number of rewarded trials in which a lick response was detected, and CR (correct rejection) is the total number of unrewarded trials in which no lick response was detected.

References

- [1] Peter A Brennan and Eric B Keverne. Something in the air? new insights into mammalian pheromones. *Current biology*, 14(2):R81–R89, 2004. doi: 10.1016/j.cub.2003.12.052.

- [2] Marcus C Stensmyr, Susanne Erland, Eric Hallberg, Rita Wallén, Peter Greenaway, and Bill S Hansson. Insect-like olfactory adaptations in the terrestrial giant robber crab. *Current Biology*, 15(2):116–121, 2005. doi: 10.1016/j.cub.2004.12.069.
- [3] Elissa A Hallem, Anupama Dahanukar, and John R Carlson. Insect odor and taste receptors. *Annu. Rev. Entomol.*, 51:113–135, 2006. doi: 10.1146/annurev.ento.51.051705.113646.
- [4] Ring T Cardé and Mark A Willis. Navigational strategies used by insects to find distant, wind-borne sources of odor. *Journal of chemical ecology*, 34:854–866, 2008. doi: 0.1007/s10886-008-9484-5.
- [5] Adil Ghani Khan, Manaswini Sarangi, and Upinder Singh Bhalla. Rats track odour trails accurately using a multi-layered strategy with near-optimal sampling. *Nature communications*, 3(1):703, 2012. doi: 10.1038/ncomms1712.
- [6] Regina M Sullivan, Donald A Wilson, Nadine Ravel, and Anne-Marie Mouly. Olfactory memory networks: from emotional learning to social behaviors. *Frontiers in behavioral neuroscience*, 9:36, 2015. doi: 10.3389/fnbeh.2015.00036.
- [7] Mohammed A Khallaf, Rongfeng Cui, Jerrit Weißflog, Maide Erdogmus, Aleš Svatoš, Hany KM Dweck, Dario Riccardo Valenzano, Bill S Hansson, and Markus Knaden. Large-scale characterization of sex pheromone communication systems in drosophila. *Nature communications*, 12(1):4165, 2021. doi: 10.1038/s41467-021-24395-z.
- [8] Jeffrey A Riffell, Leif Abrell, and John G Hildebrand. Physical processes and real-time chemical measurement of the insect olfactory environment. *Journal of chemical ecology*, 34:837–853, 2008. doi: 10.1007/s10886-008-9490-7.

- [9] Floris Van Breugel and Michael H Dickinson. Plume-tracking behavior of flying drosophila emerges from a set of distinct sensory-motor reflexes. *Current Biology*, 24(3):274–286, 2014. doi: 10.1016/j.cub.2013.12.023.
- [10] Floris Van Breugel, Jeff Riffell, Adrienne Fairhall, and Michael H Dickinson. Mosquitoes use vision to associate odor plumes with thermal targets. *Current Biology*, 25(16):2123–2129, 2015. doi: 10.1016/j.cub.2015.06.046.
- [11] Mahmut Demir, Nirag Kadakia, Hope D Anderson, Damon A Clark, and Thierry Emonet. Walking drosophila navigate complex plumes using stochastic decisions biased by the timing of odor encounters. *Elife*, 9:e57524, 2020. doi: 10.7554/eLife.57524.
- [12] Agenor Mafra-Neto and Ring T Cardé. Fine-scale structure of pheromone plumes modulates upwind orientation of flying moths. *Nature*, 369(6476):142–144, 1994. doi: 10.1038/369142a0.
- [13] Neil J Vickers, Thomas A Christensen, Thomas C Baker, and John G Hildebrand. Odour-plume dynamics influence the brain’s olfactory code. *Nature*, 410(6827):466–470, 2001. doi: 10.1038/35068559.
- [14] K. R. Mylne and P. J. Mason. Concentration fluctuation measurements in a dispersing plume at a range of up to 1000 m. *Quarterly Journal of the Royal Meteorological Society*, 117(497):177–206, 1991. ISSN 1477870X. doi: 10.1002/qj.49711749709.
- [15] Kristine A Justus, John Murlis, Chris Jones, and Ring T Cardé. Measurement of odor-plume structure in a wind tunnel using a photoionization detector and a tracer gas. *Environmental Fluid Mechanics*, 2:115–142, 2002. doi: 10.1023/A:1016227601019.
- [16] Erin G Connor, Margaret K McHugh, and John P Crimaldi. Quantification of airborne

- odor plumes using planar laser-induced fluorescence. *Experiments in Fluids*, 59:1–11, 2018. doi: 10.1007/s00348-018-2591-3.
- [17] Eugene Yee, R. Chan, P. R. Kosteniuk, G. M. Chandler, C. A. Biltoft, and J. F. Bowers. The vertical structure of concentration fluctuation statistics in plumes dispersing in the atmospheric surface layer. *Boundary-Layer Meteorology*, 76(1-2):41–67, October 1995. ISSN 0006-8314, 1573-1472. doi: 10.1007/BF00710890.
- [18] Antonio Celani, Emmanuel Villermaux, and Massimo Vergassola. Odor Landscapes in Turbulent Environments. *Physical Review X*, 4(4):041015, October 2014. ISSN 2160-3308. doi: 10.1103/PhysRevX.4.041015.
- [19] J J Hopfield. Olfactory computation and object perception. *Proceedings of the National Academy of Sciences*, 88(15):6462–6466, August 1991. ISSN 0027-8424, 1091-6490. doi: 10.1073/pnas.88.15.6462.
- [20] Agenor Mafra-Neto and Ring T. Cardé. Fine-scale structure of pheromone plumes modulates upwind orientation of flying moths. *Nature*, 369(6476):142–144, May 1994. ISSN 0028-0836, 1476-4687. doi: 10.1038/369142a0.
- [21] Michael Schmuker, Viktor Bahr, and Ramón Huerta. Exploiting plume structure to decode gas source distance using metal-oxide gas sensors. *Sensors and Actuators B: Chemical*, 235:636–646, nov 2016. doi: 10.1016/j.snb.2016.05.098.
- [22] Paul Szyszka, Richard C Gerkin, C Giovanni Galizia, and Brian H Smith. High-speed odor transduction and pulse tracking by insect olfactory receptor neurons. *Proceedings of the National Academy of Sciences*, 111(47):16925–16930, 2014. doi: 10.1073/pnas.1412051111.

- [23] Sabine Krofczik. Rapid odor processing in the honeybee antennal lobe network. *Frontiers in Computational Neuroscience*, 2, 2008. ISSN 16625188. doi: 10.3389/neuro.10.009.2008.
- [24] Teun Dekker and Ring T. Cardé. Moment-to-moment flight manoeuvres of the female yellow fever mosquito (*Aedes aegypti* L.) in response to plumes of carbon dioxide and human skin odour. *Journal of Experimental Biology*, 214(20):3480–3494, October 2011. ISSN 1477-9145, 0022-0949. doi: 10.1242/jeb.055186.
- [25] Tobias Ackels, Andrew Erskine, Debanjan Dasgupta, Alina Cristina Marin, Tom P. A. Warner, Sina Tootonian, Izumi Fukunaga, Julia J. Harris, and Andreas T. Schaefer. Fast odour dynamics are encoded in the olfactory system and guide behaviour. *Nature*, 593(7860):558–563, May 2021. doi: 10.1038/s41586-021-03514-2.
- [26] Achim J. Lilienthal, Amy Loutfi, and Tom Duckett. Airborne chemical sensing with mobile robots. *Sensors*, 6(11):1616–1678, 2006. ISSN 1424-8220. doi: 10.3390/s6111616.
- [27] Adam Francis, Shuai Li, Christian Griffiths, and Johann Sienz. Gas source localization and mapping with mobile robots: A review. *Journal of Field Robotics*, 39(8):1341–1373, 2022. doi: 10.1002/rob.22109.
- [28] James A. Covington, Santiago Marco, Krishna C. Persaud, Susan S. Schiffman, and H. Troy Nagle. Artificial Olfaction in the 21st Century. *IEEE Sensors Journal*, 21(11):12969–12990, 2021. ISSN 1530-437X. doi: 10.1109/jsen.2021.3076412.
- [29] Joseph R Stetter, Peter C Jurs, and Susan L Rose. Detection of hazardous gases and vapors: pattern recognition analysis of data from an electrochemical sensor array. *Analytical Chemistry*, 58(4):860–866, 1986. doi: 10.1021/ac00295a047.

- [30] DE Maier, R Hulasare, B Qian, P Armstrong, et al. Monitoring carbon dioxide levels for early detection of spoilage and pests in stored grain. In *Proceedings of the 9th International Working Conference on Stored Product Protection*, volume 1, page 117, 2006.
- [31] Mariana Valente Farraia, João Cavaleiro Rufo, Inês Paciência, Francisca Mendes, Luís Delgado, and André Moreira. The electronic nose technology in clinical diagnosis: A systematic review. *Porto biomedical journal*, 4(4), 2019. doi: 10.1097/j.pbj.0000000000000042.
- [32] Gyuweon Jung, Jaehyeon Kim, Seongbin Hong, Hunhee Shin, Yujeong Jeong, Wonjun Shin, Dongseok Kwon, Woo Young Choi, and Jong-Ho Lee. Energy Efficient Artificial Olfactory System with Integrated Sensing and Computing Capabilities for Food Spoilage Detection. *Advanced Science*, 10(30):2302506, October 2023. ISSN 2198-3844, 2198-3844. doi: 10.1002/advs.202302506.
- [33] Gideon Kowadlo and R Andrew Russell. Robot odor localization: a taxonomy and survey. *The International Journal of Robotics Research*, 27(8):869–894, 2008. doi: 10.1177/0278364908095.
- [34] Javier Burgués, Victor Hernández, Achim J Lilienthal, and Santiago Marco. Smelling nano aerial vehicle for gas source localization and mapping. *Sensors*, 19(3):478, 2019. doi: 10.3390/s19030478.
- [35] Tao Jing, Qing-Hao Meng, and Hiroshi Ishida. Recent progress and trend of robot odor source localization. *IEEJ Transactions on Electrical and Electronic Engineering*, 16(7): 938–953, 2021. doi: 10.1002/tee.23364.
- [36] Nirag Kadakia, Mahmut Demir, Brenden T. Michaelis, Brian D. DeAngelis, Matthew A. Reidenbach, Damon A. Clark, and Thierry Emonet. Odour motion sensing enhances nav-

- igation of complex plumes. *Nature*, 611(7937):754–761, November 2022. ISSN 0028-0836, 1476-4687. doi: 10.1038/s41586-022-05423-4.
- [37] Krishna Persaud and George Dodd. Analysis of discrimination mechanisms in the mammalian olfactory system using a model nose. *Nature*, 299(5881):352–355, 1982. doi: 10.1038/299352a0.
- [38] Frank Röck, Nicolae Barsan, and Udo Weimar. Electronic nose: current status and future trends. *Chemical reviews*, 108(2):705–725, 2008. doi: 10.1021/cr068121q.
- [39] Haotian Liu, Li Zhang, King Ho Holden Li, and Ooi Kiang Tan. Microhotplates for metal oxide semiconductor gas sensor applications—towards the cmos-mems monolithic approach. *Micromachines*, 9(11):557, 2018.
- [40] Ethan L. W. Gardner, Julian W. Gardner, and Florin Udrea. Micromachined Thermal Gas Sensors—A Review. *Sensors*, 23(2):681, January 2023. ISSN 1424-8220. doi: 10.3390/s23020681.
- [41] Daniel Rüffer, Felix Hoehne, and Johannes Bühler. New digital metal-oxide (mox) sensor platform. *Sensors*, 18(4):1052, 2018. doi: <https://doi.org/10.3390/s18041052>.
- [42] Junhan Wang, Yuezhong Lin, Ruirui Liu, and Jun Fu. Odor source localization of multi-robots with swarm intelligence algorithms: A review. *Frontiers in Neurorobotics*, 16: 949888, November 2022. ISSN 1662-5218. doi: 10.3389/fnbot.2022.949888.
- [43] Alexander Vergara, Kurt D. Benkstein, Christopher B. Montgomery, and Steve Semancik. Demonstration of fast and accurate discrimination and quantification of chemically similar species utilizing a single cross-selective chemiresistor. *Analytical Chemistry*, 86(14): 6753–6757, 2014. ISSN 15206882. doi: 10.1021/ac501490k.

- [44] Dominique Martinez, Lotfi Arhidi, Elodie Demondion, Jean-Baptiste Masson, and Philippe Lucas. Using insect electroantennogram sensors on autonomous robots for olfactory searches. *JoVE (Journal of Visualized Experiments)*, 90:e51704, 2014.
- [45] Javier G. Monroy, Javier González-Jiménez, and Jose Luis Blanco. Overcoming the Slow Recovery of MOX Gas Sensors through a System Modeling Approach. *Sensors*, 12(10):13664–13680, October 2012. ISSN 1424-8220. doi: 10.3390/s121013664.
- [46] Enrico Di Lello, Marco Trincavelli, Herman Bruyninckx, and Tinne De Laet. Augmented Switching Linear Dynamical System Model for Gas Concentration Estimation with MOX Sensors in an Open Sampling System. *Sensors*, 14(7):12533–12559, July 2014. ISSN 1424-8220. doi: 10.3390/s140712533.
- [47] D. Martinez, J. Burgués, and Santiago Marco. Fast Measurements with MOX Sensors: A Least-Squares Approach to Blind Deconvolution. *Sensors*, 19(18):4029, September 2019. ISSN 1424-8220. doi: 10.3390/s19184029.
- [48] Javier Burgues and Santiago Marco. Wind-Independent Estimation of Gas Source Distance From Transient Features of Metal Oxide Sensor Signals. *IEEE Access*, 7:140460–140469, 2019. ISSN 2169-3536. doi: 10.1109/ACCESS.2019.2940936.
- [49] Javier Burgues, Luis F. Valdez, and Santiago Marco. High-bandwidth e-nose for rapid tracking of turbulent plumes. In *2019 IEEE International Symposium on Olfaction and Electronic Nose (ISOEN)*, pages 1–3. IEEE, May 2019. ISBN 978-1-5386-8327-9. doi: 10.1109/ISOEN.2019.8823158.
- [50] Yuxin Xing, Timothy A Vincent, Marina Cole, and Julian W Gardner. Real-time thermal modulation of high bandwidth MOX gas sensors for mobile robot applications. *Sensors*, 19(5):1180, 2019. doi: 10.3390/s19051180.

- [51] Damien Drix and Michael Schmuker. Resolving fast gas transients with metal oxide sensors. *ACS Sensors*, 6(3):688–692, February 2021. doi: 10.1021/acssensors.0c02006.
- [52] Sepideh Pashami, Achim Lilienthal, and Marco Trincavelli. Detecting Changes of a Distant Gas Source with an Array of MOX Gas Sensors. *Sensors*, 12(12):16404–16419, November 2012. ISSN 1424-8220. doi: 10.3390/s121216404.
- [53] Guillem Domènech-Gil, Nguyen Thanh Duc, J. Jacob Wikner, Jens Eriksson, Sören Nilsson Påledal, Donatella Puglisi, and David Bastviken. Electronic Nose for Improved Environmental Methane Monitoring. *Environmental Science & Technology*, 58(1):352–361, January 2024. ISSN 0013-936X, 1520-5851. doi: 10.1021/acs.est.3c06945.
- [54] Javier Burgués and Santiago Marco. Environmental chemical sensing using small drones: A review. *Science of The Total Environment*, 748:141172, December 2020. ISSN 00489697. doi: 10.1016/j.scitotenv.2020.141172.
- [55] Mykhail Tereshkov, Tetiana Dontsova, Bilge Saruhan, and Svitlana Krüger. Metal Oxide-Based Sensors for Ecological Monitoring: Progress and Perspectives. *Chemosensors*, 12(3):42, March 2024. ISSN 2227-9040. doi: 10.3390/chemosensors12030042.
- [56] Lingxiao Wang, Shuo Pang, Mantasha Noyela, Kevin Adkins, Lulu Sun, and Marwa El-Sayed. Vision and olfactory-based wildfire monitoring with uncrewed aircraft systems. In *2023 20th International Conference on Ubiquitous Robots (UR)*, pages 716–723, 2023. doi: 10.1109/UR57808.2023.10202419.
- [57] Han Fan, Victor Hernandez Bennetts, Erik Schaffernicht, and Achim Lilienthal. Towards Gas Discrimination and Mapping in Emergency Response Scenarios Using a Mobile Robot with an Electronic Nose. *Sensors*, 19(3):685, February 2019. ISSN 1424-8220. doi: 10.3390/s19030685.

- [58] Alina Cristina Marin, Andreas T Schaefer, and Tobias Ackels. Spatial information from the odour environment in mammalian olfaction. *Cell and Tissue Research*, 383(1):473–483, January 2021. ISSN 0302-766X, 1432-0878. doi: 10.1007/s00441-020-03395-3.
- [59] Debanjan Dasgupta, Tom P. A. Warner, Andrew Erskine, and Andreas T. Schaefer. Coupling of mouse olfactory bulb projection neurons to fluctuating odor pulses. *Journal of Neuroscience*, 42(21):4278–4296, 2022. ISSN 0270-6474. doi: 10.1523/JNEUROSCI.1422-21.2022.
- [60] Satoshi Nakata and Naho Takahara. Characteristic nonlinear responses of a semiconductor gas sensor to hydrocarbons and alcohols under the combination of cyclic temperature and continuous flow. *Sensors and Actuators B: Chemical*, 307:127635, 2020.
- [61] Davide Di Giuseppe, Alexandro Catini, Elisabetta Comini, Dario Zappa, Corrado Di Natale, and Eugenio Martinelli. Optimizing MOX sensor array performances with a reconfigurable self-adaptive temperature modulation interface. *Sensors and Actuators B: Chemical*, 333:129509, 2021.
- [62] Satoshi Nakata and Naho Takahara. Distinction of gaseous mixtures based on different cyclic temperature modulations. *Sensors and Actuators B: Chemical*, 359:131615, 2022. doi: 10.1016/j.snb.2022.131615.
- [63] Fanli Meng, Xi Luan, Chunjin Mi, Hanyang Ji, Hongmin Zhu, and Zhenyu Yuan. Recognition algorithm for detection of precursor chemicals by semiconductor gas sensor array under dynamic measurement. *IEEE Sensors Journal*, 23(3):1818–1826, 2023. doi: 10.1109/JSEN.2022.3232179.
- [64] Nik Dennler, Damien Drix, Shavika Rastogi, André van Schaik, and Michael Schmuker. Rapid inference of geographical location with an event-based electronic nose. In *Proceed-*

- ings of the 2022 Annual Neuro-Inspired Computational Elements Conference, NICE '22*, page 112–114. Association for Computing Machinery, 2022. ISBN 9781450395595. doi: 10.1145/3517343.3517381.
- [65] Damien Drix, Nik Dennler, and Michael Schmuker. Rapid recognition of olfactory scenes with a portable mox sensor system using hotplate modulation. In *2022 IEEE International Symposium on Olfaction and Electronic Nose (ISOEN)*, pages 1–4, 2022. doi: 10.1109/ISOEN54820.2022.9789654.
- [66] Adam Kepecs, Naoshige Uchida, and Zachary F. Mainen. The Sniff as a Unit of Olfactory Processing. *Chemical Senses*, 31(2):167–179, February 2006. ISSN 1464-3553, 0379-864X. doi: 10.1093/chemse/bjj016.
- [67] C. Giovanni Galizia and Wolfgang Rössler. Parallel Olfactory Systems in Insects: Anatomy and Function. *Annual Review of Entomology*, 55(1):399–420, January 2010. ISSN 0066-4170, 1545-4487. doi: 10.1146/annurev-ento-112408-085442.
- [68] Michael Schmuker, Nobuhiro Yamagata, Martin Paul Nawrot, and Randolph Menzel. Parallel Representation of Stimulus Identity and Intensity in a Dual Pathway Model Inspired by the Olfactory System of the Honeybee. *Frontiers in Neuroengineering*, 4, 2011. ISSN 1662-6443. doi: 10.3389/fneng.2011.00017.
- [69] Dan Rokni, Vivian Hemmelder, Vikrant Kapoor, and Venkatesh N Murthy. An olfactory cocktail party: figure-ground segregation of odorants in rodents. *Nature Neuroscience*, 17(9):1225–1232, September 2014. ISSN 1097-6256, 1546-1726. doi: 10.1038/nn.3775.
- [70] Bardienus P. Duisterhof, Shushuai Li, Javier Burgues, Vijay Janapa Reddi, and Guido C. H. E. De Croon. Sniffy Bug: A Fully Autonomous Swarm of Gas-Seeking Nano Quadcopters in Cluttered Environments. In *2021 IEEE/RSJ International Conference on*

- Intelligent Robots and Systems (IROS)*, pages 9099–9106. IEEE, September 2021. ISBN 978-1-66541-714-3. doi: 10.1109/IROS51168.2021.9636217.
- [71] Julio Torres-Tello, Ana V. Guaman, and Seok-Bum Ko. Improving the detection of explosives in a mox chemical sensors array with lstm networks. *IEEE Sensors Journal*, 20(23):14302–14309, 2020. doi: 10.1109/JSEN.2020.3007431.
- [72] Mohammad F. Tariq, Suzanne M. Lewis, Aliena Lowell, Sidney Moore, Jesse T. Miles, David J. Perkel, and David H. Gire. Using Head-Mounted Ethanol Sensors to Monitor Olfactory Information and Determine Behavioral Changes Associated with Ethanol-Plume Contact during Mouse Odor-Guided Navigation. *eneuro*, 8(1):ENEURO.0285–20.2020, January 2021. ISSN 2373-2822. doi: 10.1523/ENEURO.0285-20.2020.
- [73] Carver Mead. Neuromorphic electronic systems. *Proceedings of the IEEE*, 78(10):1629–1636, 1990. doi: 10.1109/5.58356.
- [74] Giacomo Indiveri, Bernabé Linares-Barranco, Tara Julia Hamilton, André van Schaik, Ralph Etienne-Cummings, Tobi Delbruck, Shih Chii Liu, Piotr Dudek, Philipp Häfliger, Sylvie Renaud, Johannes Schemmel, Gert Cauwenberghs, John Arthur, Kai Hynna, Fopofolu Folowosele, Sylvain Saighi, Teresa Serrano-Gotarredona, Jayawan Wijekoon, Yingxue Wang, and Kwabena Boahen. Neuromorphic silicon neuron circuits. *Frontiers in Neuroscience*, 5(MAY):1–23, 2011. ISSN 16624548. doi: 10.3389/fnins.2011.00073.
- [75] Patrick Lichtsteiner, Christoph Posch, and Tobi Delbruck. A 128×128 120 db 15 μ s latency asynchronous temporal contrast vision sensor. *IEEE journal of solid-state circuits*, 43(2):566–576, 2008.
- [76] Shih-Chii Liu and Tobi Delbruck. Neuromorphic sensory systems. *Current opinion in neurobiology*, 20(3):288–295, 2010. doi: 10.1016/j.conb.2010.03.007.

- [77] Krishna C Persaud, Santiago Marco, and Agustin Gutierrez-Galvez. *Neuromorphic olfaction*. CRC Press, 2013.
- [78] Elisabetta Chicca, Michael Schmuker, and Martin P Nawrot. Neuromorphic sensors, olfaction. *10.1016/j.conb.2010.03.007*, 2014. doi: 10.1016/j.conb.2010.03.007.
- [79] Shavika Rastogi, Nik Dennler, Michael Schmuker, and André van Schaik. Spike-time encoding of gas concentrations using neuromorphic analog sensory front-end. In *2023 IEEE Biomedical Circuits and Systems Conference (BioCAS)*, pages 1–5, 2023. doi: 10.1109/BioCAS58349.2023.10388752.
- [80] Loic Laplatine, Maryse Fournier, Nicolas Gaignebet, Yanxia Hou, Raphael Mathey, Cyril Herrier, Jie Liu, Delphine Descloux, Bertrand Gautheron, and Thierry Livache. Silicon photonic olfactory sensor based on an array of 64 biofunctionalized Mach-Zehnder interferometers. *Optics Express*, 30(19):33955, September 2022. ISSN 1094-4087. doi: 10.1364/OE.461858.
- [81] Chen Wang, Zhesi Chen, Chak Lam Jonathan Chan, Zhu’an Wan, Wenhao Ye, Wenying Tang, Zichao Ma, Beitao Ren, Daquan Zhang, Zhilong Song, and others. Biomimetic olfactory chips based on large-scale monolithically integrated nanotube sensor arrays. *Nature Electronics*, pages 1–11, 2024. doi: 10.1038/s41928-023-01107-7. Publisher: Nature Publishing Group UK London.
- [82] Greg Welch, Gary Bishop, and others. An introduction to the Kalman filter. 1995. Publisher: Chapel Hill, NC, USA.
- [83] Fabio Rastrello, Pisana Placidi, Luca Abbati, Andrea Scorzoni, Enrico Cozzani, Ivan Elmi, Stefano Zampolli, Gian Carlo Cardinali, et al. Thermal transient measurements of an ultra-low-power MOX sensor. *Journal of Sensors*, 2010, 2010. doi: 10.1155/2010/493765.

- [84] Jean-Philippe Vert, Koji Tsuda, and Bernhard Schölkopf. A primer on kernel methods. *Kernel methods in computational biology*, 47:35–70, 2004. doi: 10.7551/mitpress/4057.003.0004.
- [85] James W Cooley and John W Tukey. An algorithm for the machine calculation of complex fourier series. *Mathematics of computation*, 19(90):297–301, 1965.
- [86] Tin Kam Ho. Random decision forests. In *Proceedings of 3rd International Conference on Document Analysis and Recognition*, volume 1, pages 278–282 vol.1, 1995. doi: 10.1109/ICDAR.1995.598994.
- [87] Andrew Erskine, Thorsten Bus, Jan T Herb, and Andreas T Schaefer. Autonomouse: High throughput operant conditioning reveals progressive impairment with graded olfactory bulb lesions. *PLoS One*, 14(3):e0211571, 2019. doi: 10.1371/journal.pone.0211571.

Acknowledgements

The authors would like to thank Y. Zhang for assisting with the odourant samples, as well as M. Psarrou, S. Sutton, Y. Bethi, N. Ralph and P. Hurley for fruitful discussions.

Funding

Part of this work was funded by an NSF/MRC award under the Next Generation Networks for Neuroscience initiative (NeuroNex Odor to action, NSF #2014217, MRC #MR/T046759/1). Part of this work was supported by a Boehringer Ingelheim Fonds PhD fellowship to CDC.

Author contributions statement

MS, AS, ND, DD, TW, SR and AvS conceptualised the study. DD designed the electronic nose hardware. DD and ND developed the electronic nose software. ND, DD, TW, SR and CDC

conducted the investigations and experiments. ND and DD performed formal analysis. ND created the visualisations. MS, AS and AvS acquired funding. ND drafted the original writing. Everyone participated in the review and editing process.

Competing interests

The authors declare no competing interests.

Supplementary Materials

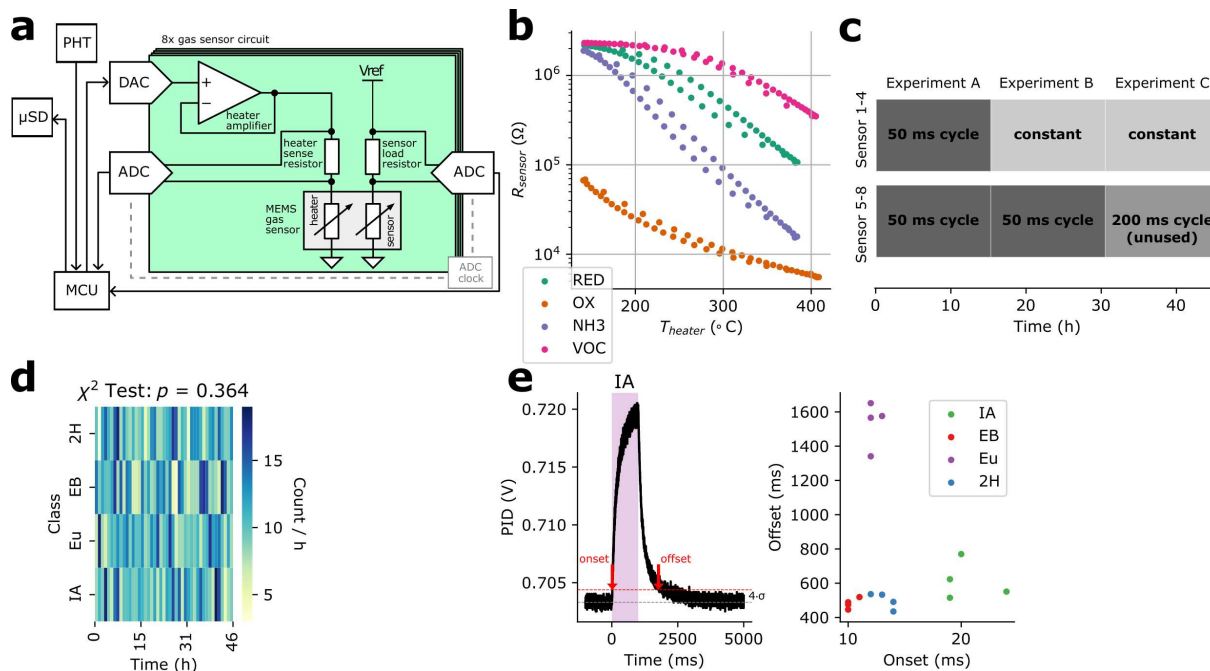


Figure S1: **Supplementary figure for experimental setup.** **a**, Electronic nose design, displaying how the microcontroller unit (MCU) sets and reads out the sensor heaters in a closed loop, while reading out the analyte dependent sensor resistances. Further, the MCU connects to an environmental sensor (PHT) and a micro SD card. **b**, R-T curve of a 50 ms temperature cycle between 150 °C and 400 °C without external stimulus, displaying how the sensor response closely follows the hotplate temperature. **c**, Different sensor hotplate settings over time. For each experiments, all the stimuli were presented in randomised order. **d**, Heatmap depicting the distribution of odour presentations over a set of 1 hour time intervals. A χ^2 test was performed to assess the randomness of class distribution over time intervals, with the computed p-value indicated as 'p'. **e**, PID response to a 1 s isoamyl acetate pulse. Grey-dotted and red dotted lines denote mean of pre-stimulus baseline and 4 standard deviations threshold respectively. Where the response crosses the threshold upwards (downwards), the odour onset (offset) is registered. **f**, Extracted odour onsets (w.r.t. $t = 0$ ms) and offsets (w.r.t. $t = 1000$ ms) for 1000 ms pulses of different odours. For all experiments, the odourants are abbreviated as follows. IA: isoamyl acetate; EB: ethyl butyrate; Eu: cineol; 2H: 2-heptanone; blank: odourless control.

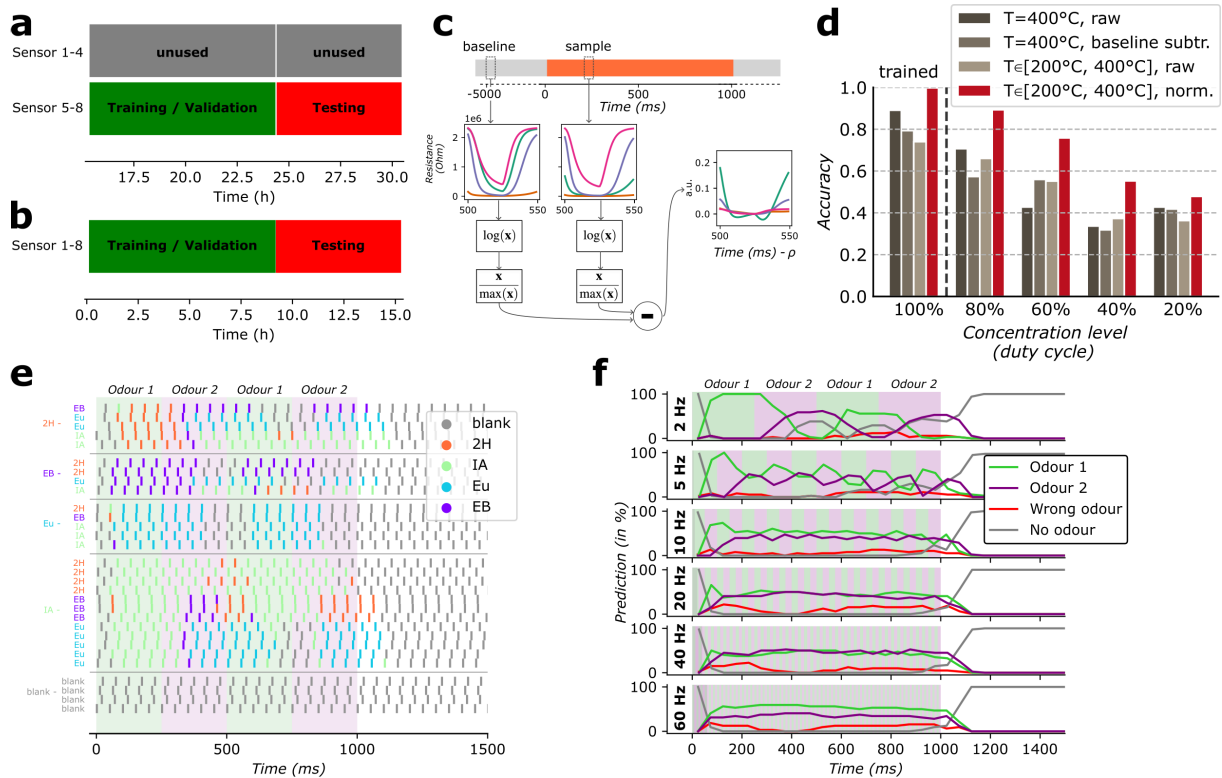


Figure S2: Supplementary figure for fast odour classification. **a**, Data splitting for robustness analysis of the rapid heater modulation data features (see Fig. 2e). **b**, Data splitting for evaluating the dynamic classification of millisecond odour pulses (see Fig. 3). **c**, Normalisation procedure for the heater modulation data feature. Time shifted by cycle phase ρ w.r.t. odour onset, for visual guidance only. **d**, Accuracy scores for a k-nearest neighbours (k-NN) classifier trained on 50 ms data features from 1000 ms odour pulses at full concentration, and tested on 50 ms features from 1000 ms odour pulses at different concentration levels (tuned by adjusting the duty cycle of the micro-valves). Features are compared for constant heater sensor readings (raw and baseline-normalised) and cycled heater sensor readings (raw and normalised, as described in c)) **e**, Odour stimulus classification for anti-correlated odour patterns over time. An RBF-kernel SVM classifier was trained on 50 ms features from 1000 ms odour pulses, and tested on odour anti-correlated odour patterns of various frequencies. Shown here is a 2 Hz pattern. **f**, Classification correctness over time (evaluated via the true odour presence), for anti-correlated odour patterns of different switching frequencies.

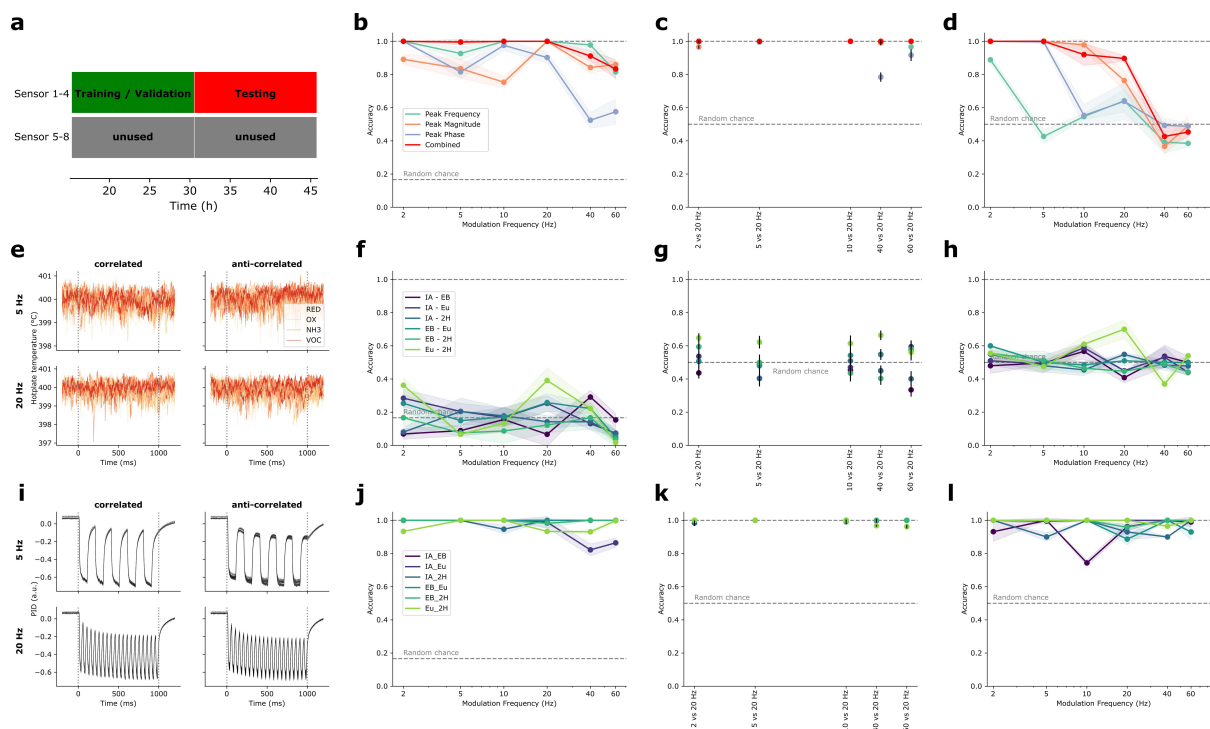


Figure S3: Supplementary figure for temporal pattern discrimination. **a**, Data splitting for evaluating the temporal pattern discrimination performance (see Fig. 4). **b-d**, Validation accuracy plots for different extracted DFT-spectrogram peak features using the MOx gas sensor resistances. **b**, Modulation frequency classification, **c**, pairwise modulation frequency classification, and **d**, correlated vs anti-correlated modulation discrimination. **e**, MOx heater temperature values for different odour modulations. Here shown are data for the odour pair IA (isoamyl acetate)- EB (ethyl butyrate), 5 trials each for 5 Hz correlated, 5 Hz anti-correlated, 20 Hz correlated and 20 Hz anti-correlated respectively. **f-h**, Test accuracy plots for different odour pair modulations, using the MOx heater temperature values. **i**, Photoionisation Detector (PID) responses for different odour modulations (odour stimuli as in **e**). **j-l**, Test accuracy plots for different odour pair modulations, using the Photoionisation Detector (PID) responses. For all the classification tasks, an ensemble of Random Forest Classifiers was used. The mean and error estimations arise from repeating training and testing with different random seeds.